

# Characterization of nickel-based microlattice materials with structural hierarchy from the nanometer to the millimeter scale

A. Torrents<sup>a</sup>, T.A. Schaedler<sup>b</sup>, A.J. Jacobsen<sup>b</sup>, W.B. Carter<sup>b</sup>, L. Valdevit<sup>a,\*</sup>

<sup>a</sup> Department of Mechanical and Aerospace Engineering, University of California, Irvine, CA 92697, USA

<sup>b</sup> HRL Laboratories LLC, Malibu, CA 90265, USA

Received 8 November 2011; received in revised form 25 January 2012; accepted 3 March 2012

Available online 7 April 2012

## Abstract

Novel nickel-based microlattice materials with structural hierarchy spanning three different length scales (nm,  $\mu\text{m}$ , mm) are characterized microstructurally and mechanically. These materials are produced by plating a sacrificial template obtained by self-propagating photopolymer waveguide prototyping. Ni–P films with a thickness of 120 nm to 3  $\mu\text{m}$  are deposited by electroless plating, whereas thicker films (5–26  $\mu\text{m}$ ) are obtained by subsequent electrodeposition of a pure Ni layer. This results in cellular materials spanning three orders of magnitude in relative density, from 0.01% to 8.5%. The thin electroless Ni–P films have ultra-fine grain size (7 nm) and a yield strength of  $\sim 2.5$  GPa, whereas the thicker electrodeposited Ni films exhibit a much broader distribution with average grain size of 116 nm and strong (100) texture in the plating direction, resulting in a yield strength of  $\sim 1$  GPa. Uniaxial compression experiments reveal two distinct mechanical responses. At ultra-low densities ( $< 0.1\%$ ), these lattices exhibit nearly full recovery after strains up to more than 50%, and damping coefficients an order of magnitude larger than for conventional Ni foams. At higher densities (0.1–10%), the compression behavior is fully plastic, similar to traditional cellular metals. A simple mechanical analysis reveals that the transition occurs when the thickness-to-diameter ratio of the truss elements is of the order of the yield strain of the material, in agreement with experimental observations. Optical and electron imaging of deformed lattices show that the deformation largely localizes around the nodes. In the ultra-light regime, the microlattice materials are stiffer and stronger than any existing alternative.

© 2012 Acta Materialia Inc. Published by Elsevier Ltd. All rights reserved.

**Keywords:** Microlattice materials; Cellular materials; Mechanical characterization; EBSD; Nanocrystalline nickel

## 1. Introduction

Over the past decade, cellular metallic structures have emerged as a new class of materials with low density and superior mechanical, electrical, thermal, and acoustic properties [1–3]. Applications range from lightweight structures to impact protection, sound absorption and active cooling [4–6]. The properties of cellular materials are naturally dependent upon the choice of the parent material and the topology of the architecture. From a topological standpoint, cellular materials can be categorized as either open or closed, with either a stochastic or an ordered structure.

When loaded macroscopically (e.g., in uniaxial compression), stochastic cellular materials respond by bending deformation at the ligament level, resulting in an elastic modulus,  $E$ , which scales with  $(\rho/\rho_s)^2$ , and a yield strength,  $\sigma_Y$ , which scales with  $(\rho/\rho_s)^{3/2}$  [1]. Here,  $\rho$  and  $\rho_s$  represent the effective density of the lattice and the density of the base material, respectively. Both elastic modulus and strength of the lattice can be significantly increased if the structure is ordered instead of stochastic: a fully triangulated truss-type architecture deforms primarily by axial stretching of the truss elements, allowing modulus and strength to scale linearly with the relative density [7,8].

Ordered truss-like lattices, with the smallest dimension typically in the order of millimeters, can be manufactured with a variety of techniques [3,9]. In principle, substantial

\* Corresponding author. Tel.: +1 949 824 4173; fax: +1 949 824 8585.  
E-mail address: [valdevit@uci.edu](mailto:valdevit@uci.edu) (L. Valdevit).

improvements in the mechanical properties of lattice materials are expected if the minimum characteristic dimension is reduced to the micron and sub-micron scale, by virtue of well-known size effects in the plastic flow of metals [6,10,11]. However, very few manufacturing approaches exist that allow dimensional control over six orders of magnitude (from  $\sim 100$  nm to  $\sim 10$  cm). Three-dimensional digital manufacturing of a sacrificial polymeric preform followed by metal deposition and removal of the preform is one option, as is a stacking process of photolithographically defined layers. The former approach was recently demonstrated (albeit without polymer removal), resulting in electrodeposited nickel/acrylic hybrid trusses with relative densities of 1.5–5% (relative to nickel), and good mechanical properties [12]. Both techniques are extremely slow, though, and are not feasible for the manufacture of large-scale parts ( $\sim 10$  cm or more). Recently, a new high-throughput fabrication technique for the manufacture of polymeric lattices was developed by Jacobsen et al. [13]. The approach uses an interconnected pattern of self-propagating polymer waveguides to create highly ordered cellular truss topologies. Lattices with macroscopic dimensions in the 10 cm scale and individual truss member diameters on the order of 50–100  $\mu\text{m}$  are readily obtained in less than 1 min. Conformal coating of these lattices with a metallic or ceramic film, and subsequent removal of the polymeric substrate, result in all-metallic hollow microlattices with the finest characteristic dimension (the wall thickness) as small as  $\sim 100$  nm. This technique was recently adopted to create the lightest material ever demonstrated [14].

In this paper, we present a complete microstructural and mechanical characterization of nickel microlattices produced with the technique described above, expanding upon a previously published assessment [14]. A number of samples are produced, with relative densities spanning three orders of magnitude (from 0.01% to 8.4%). The effect of the base material is decoupled from that of the topology through experimental investigations at the nano- and macroscale.

The manufacturing approach is summarized in Section 2. Section 3 describes the microstructural characterization studies for two different base materials (electroless Ni-P and electrodeposited Ni, henceforth denoted as EN Ni and ED Ni, respectively). The mechanical characterization, both at the nano- and macroscale, is presented in Section 4. Section 5 analyzes the mechanical performance of these novel microlattices and confronts it with the performance of alternative cellular materials. Conclusions follow.

## 2. Material fabrication

The nickel microlattices were fabricated at HRL Laboratories with a three-step process: (i) fabrication of a sacrificial polymeric template, (ii) coating of the template with electroless Ni deposition, possibly followed by Ni electroplating, and (iii) removal of the sacrificial template. Thiol-ene microlattice samples were fabricated from an interconnected pattern of self-propagating photopolymer waveguides as described in detail elsewhere [15,16]. The polymer microlattice samples were then used as direct templates for electroless nickel plating using a commercially available process (OM Group Inc., Cleveland, OH). Prior to electroless plating, all samples were thermally post-cured at 120  $^{\circ}\text{C}$  in air for 12 h. To prepare the surface for electroless deposition, the samples were first immersed in an aqueous solution of potassium permanganate and sodium hydroxide, then palladium catalyst was deposited by immersion in activator solution containing hydrochloric acid and tin(II) chloride (Fidelity 1018, OM Group Inc.), followed by an etch in accelerator solution containing fluoboric acid (Fidelity 1019, OM Group Inc.). The samples were then immersed in electroless nickel plating solution with nickel sulfate as nickel source, sodium hypophosphite as reducing agent, and sodium malate and acetic acid as complexing agents (9026 M, OM Group Inc.). The electroless nickel plating bath was kept at pH 4.9 by the addition of ammonium hydroxide and plating was performed at 80  $^{\circ}\text{C}$ . For electroless Ni samples, the plating time was adjusted to achieve the desired coating thickness. A wall thickness  $t$  of 500 nm was achieved by electroless nickel plating of  $\sim 3$  min. For electrodeposited Ni samples (henceforth referred to as ED Ni), the electroless deposition process was limited to 3 min, sufficient to obtain a well-conducting metallic layer on the surface of the template, and electroplating was adopted to achieve the desired film thickness. Nickel electroplating was performed using a commercial nickel sulfamate plating bath (Caswell Inc., Lyons, NY). Samples were plated between two nickel sheet anodes at 46  $^{\circ}\text{C}$ , pH 4 and a constant current density of 10  $\text{mA cm}^{-2}$ . The chemical composition of the two materials (electroless and electrodeposited nickel) was inevitably different, as discussed in Section 3. After nickel deposition the top and bottom surfaces of each sample were sanded to expose the underlying polymer at each node. The polymer was then chemically etched in a base solution (3 M NaOH at 60  $^{\circ}\text{C}$ ) for 24 h, resulting in hollow tube nickel microlattice samples (Fig. 1). A number of samples were produced

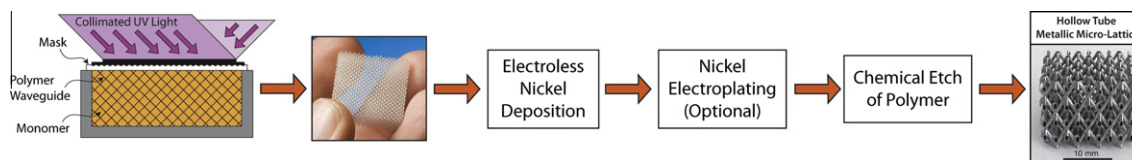


Fig. 1. Schematic of the fabrication process for nickel hollow microlattices. Details in Refs. [13,14].

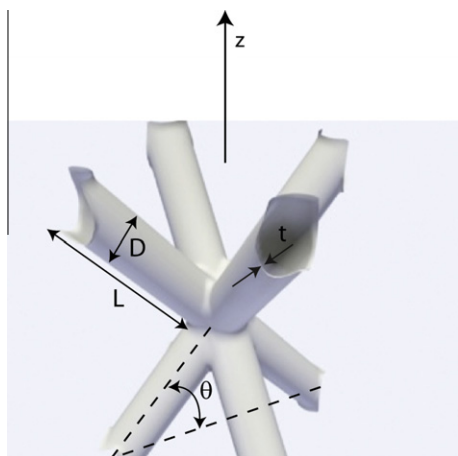


Fig. 2. Unit cell topology and definition of dimensional parameters for hollow microlattices.

with this technique, spanning three orders of magnitude in relative density (from 0.01% to 8.4%). All sample dimensions are provided in Table 1. The angle, strut length and strut diameter are nominal values, known with an accuracy of  $\pm 2^\circ$ ,  $\pm 3\%$  and  $\pm 15\%$ , respectively. The larger uncertainty on the diameter is due to the fact that struts are typically narrower at the center than at the nodes;  $D$  represents an average value. The strut thickness is measured by electron microscopy; although the technique allows a resolution of the order of nanometers, a typical variation of  $\pm 10\%$  within a sample is generally observed, for a given deposition time. Standard error analysis indicates an uncertainty of 18% on  $t/D$ . The density is measured by measuring the weight and the dimensions of the sample, resulting in an accuracy of  $\sim 10\%$ .

### 3. Microstructural characterization

#### 3.1. Electroless nickel (EN Ni) microlattices

The microstructural characterization of EN Ni films deposited on flat substrates with a process identical to that described in Section 2 has been published elsewhere [17], with two key results: (i) energy dispersive spectroscopic analysis (EDS) revealed a 93% Ni–7% P composition by weight, which was expected given the nature of the deposition bath (Section 2); (ii) a consistent grain size of  $\sim 7$  nm was determined from transmission electron microscopy (TEM) as shown in Fig. 4a and b. Grain sizes were determined by matching the total of 70 grains from five different dark-field images to circles of equivalent area. Amorphous regions in the deposit are certainly possible, but were not clearly identified in TEM imaging. Scherrer's analysis on X-ray diffraction (XRD) peaks suggests a smaller grain size (3–4 nm), fairly uniform for films with thickness between 150 and 500 nm. As it is well known that the accuracy of Scherrer's analysis is significantly reduced when the grain size is dropped below 10 nm [17], the TEM measurement

of 7 nm is assumed correct. Additional XRD analyses have been carried out in the present study (with the procedure described in Section 3.2), simply, to reveal qualitative differences with electrodeposited samples (see Section 3.2).

#### 3.2. Electrodeposited nickel (ED Ni) microlattices

##### 3.2.1. Grain size characterization

ED Ni microlattices with  $\sim 26 \mu\text{m}$  film thickness were characterized by XRD and TEM to gather information on the grain size distribution. XRD was carried out on a Siemens D5000 diffractometer equipped with graphite monochromator, using copper  $K_\alpha$  ( $\lambda = 0.15406$  nm) radiation. General scans with a step size of  $0.02^\circ$  ( $2\theta$ ) and a step time of 2 s were used for crystal size determination. A grain size of  $23.8 \pm 3$  nm was extracted with the integral breadth (IB) method [18], based on the four face-centered-cubic (fcc) diffraction peaks of Ni ((111), (200), (220), (311)). By comparison, EN Ni films show much broader and weaker peaks (Fig. 3), consistent with their much smaller grain size ( $\sim 7$  nm) and some internal lattice disorder associated with the presence of P in solid solution (Section 3.1). The coexistence of small nano-crystalline regions and amorphous regions in Ni–7% P has been previously observed [19,20]. ED Ni grain size and grain size distribution measurements were also conducted using a Philips CM 20 transmission electron microscope at 200 kV. Samples were prepared by a liftout procedure via an Omniprobe manipulator inside an FEI 3-D Quanta focused ion beam (FIB). The grain size was extracted by the Feret diameter of 80 grains from 10 different bright field images using the ImageJ software package. The average grain size was found to be 116 nm, with a standard deviation of 52 nm and a round factor of 0.68, indicating a very broad and almost bimodal distribution (Fig. 4c and d). The discrepancy between XRD and TEM grain size estimation (with XRD predicting a much smaller grain size) is attributed to the broad and binomial distribution, as previously reported in the literature. The accuracy of XRD grain measurements has previously been questioned for samples with an inhomogeneous distribution of grain size and for sizes  $> 100$  nm [21–24]. The implication is that XRD cannot be used for grain size determination of ED Ni microtrusses, and the more elaborate TEM approach is required.

##### 3.2.2. Texture analysis

ED Ni XRD profiles show a strong (200) texture (Fig. 3). Texture on ED films is well known and is mainly attributed by the presence of impurities in the electrolyte bath, which enhance the strength of the (100) texture by reducing the (100) surface energy [22,24–26]. Rashidi et al. [27,28] reported that ED Ni deposited under the same conditions ( $i = 12.5 \text{ mA cm}^{-2}$ ) results in films with an average grain size of  $\sim 180$  nm and with a strong (200) texture, in good agreement with our results. The texture can be usually quantified from XRD spectra by analyzing peak intensity ratios. However, this approach is not reliable on

Table 1  
Summary of architecture and properties of tested microlattices.

Sample	Wall thickness $t$ ( $\mu\text{m}$ )	Strut diameter $D$ ( $\mu\text{m}$ )	$t/D$	Strut length $L$ ( $\mu\text{m}$ )	Strut angle ( $^\circ$ )	Density (mg/cc)	Relative density (%)	Compressive strength $\sigma_y$ (kPa)	Compressive modulus $E$ (GPa)	Residual strain	Energy loss coeff. 1st cycle
A	$26.00 \pm 2.6$	$175 \pm 26$	$(1.5 \pm 0.3)\text{E}-1$	$1200 \pm 36$	$60 \pm 2$	$752.00 \pm 75.20$	$8.45 \pm 1.27$	$8510 \pm 25$	$0.58 \pm 0.003$	$0.46 \pm 0.01$	
B	$26.00 \pm 2.6$	$175 \pm 26$	$(1.5 \pm 0.3)\text{E}-1$	$1200 \pm 36$	$60 \pm 2$	$750.00 \pm 75.00$	$8.43 \pm 1.26$	$8560 \pm 25$	$0.57 \pm 0.003$	$0.46 \pm 0.01$	
C	$1.40 \pm 0.14$	$150 \pm 23$	$(1.9 \pm 0.4)\text{E}-2$	$1050 \pm 32$	$60 \pm 2$	$43.06 \pm 4.31$	$0.54 \pm 0.08$	$120.8 \pm 12.5$	$(9.2 \pm 0.1)\text{E}-3$	$0.34 \pm 0.02$	
D	$1.40 \pm 0.14$	$150 \pm 23$	$(1.9 \pm 0.4)\text{E}-2$	$1050 \pm 32$	$60 \pm 2$	$43.06 \pm 4.31$	$0.54 \pm 0.08$	$145.3 \pm 12.5$	$(9.0 \pm 0.1)\text{E}-3$	$0.30 \pm 0.02$	
E	$3.50 \pm 0.35$	$400 \pm 60$	$(7.0 \pm 1.3)\text{E}-3$	$4000 \pm 120$	$60 \pm 2$	$22.65 \pm 2.26$	$0.28 \pm 0.04$	$17.7 \pm 2.5$	$(9.1 \pm 1.5)\text{E}-4$	$0.38 \pm 0.02$	
F	$0.55 \pm 0.06$	$160 \pm 24$	$(3.4 \pm 0.6)\text{E}-3$	$1050 \pm 32$	$60 \pm 2$	$17.14 \pm 1.71$	$0.21 \pm 0.03$	$19.6 \pm 2.5$	$(1.3 \pm 0.15)\text{E}-3$	$0.097 \pm 0.015$	
G	$0.55 \pm 0.06$	$160 \pm 24$	$(3.4 \pm 0.6)\text{E}-3$	$1050 \pm 32$	$60 \pm 2$	$17.14 \pm 1.71$	$0.21 \pm 0.03$	$14.2 \pm 2.5$	$(1.0 \pm 0.15)\text{E}-3$	$0.070 \pm 0.015$	
H	$0.50 \pm 0.05$	$170 \pm 26$	$(2.9 \pm 0.5)\text{E}-3$	$817 \pm 25$	$50 \pm 2$	$16.59 \pm 1.66$	$0.21 \pm 0.03$	$10.1 \pm 1.5$	$(5.7 \pm 1.5)\text{E}-4$	–	
I	$0.55 \pm 0.06$	$140 \pm 21$	$(3.9 \pm 0.7)\text{E}-3$	$1050 \pm 32$	$60 \pm 2$	$16.20 \pm 1.62$	$0.20 \pm 0.03$	$12.1 \pm 2.5$	$(7.1 \pm 1.5)\text{E}-4$	$0.090 \pm 0.015$	
J	$0.50 \pm 0.05$	$170 \pm 26$	$(2.9 \pm 0.5)\text{E}-3$	$817 \pm 25$	$50 \pm 2$	$15.16 \pm 1.52$	$0.19 \pm 0.03$	$10.0 \pm 1.5$	$(5.3 \pm 1.5)\text{E}-4$	$0.026 \pm 0.020$	$0.80 \pm 0.08$
K	$0.50 \pm 0.05$	$170 \pm 26$	$(2.9 \pm 0.5)\text{E}-3$	$817 \pm 25$	$50 \pm 2$	$14.51 \pm 1.45$	$0.18 \pm 0.03$	$8.9 \pm 1.5$	$(3.4 \pm 1.5)\text{E}-4$	–	
L	$0.50 \pm 0.05$	$170 \pm 26$	$(2.9 \pm 0.5)\text{E}-3$	$817 \pm 25$	$50 \pm 2$	$14.14 \pm 1.41$	$0.18 \pm 0.03$	$9.1 \pm 1.5$	$(6.3 \pm 1.5)\text{E}-4$	–	$0.43 \pm 0.04$
M	$0.50 \pm 0.05$	$170 \pm 26$	$(2.9 \pm 0.5)\text{E}-3$	$817 \pm 25$	$50 \pm 2$	$13.01 \pm 1.30$	$0.16 \pm 0.02$	$7.1 \pm 1.5$	$(3.3 \pm 1.5)\text{E}-4$	–	$0.33 \pm 0.03$
N	$0.25 \pm 0.03$	$120 \pm 18$	$(2.1 \pm 0.4)\text{E}-3$	$675 \pm 20$	$60 \pm 2$	$11.20 \pm 1.12$	$0.14 \pm 0.02$	$5.0 \pm 1.0$	$(1.8 \pm 0.5)\text{E}-4$	$0.005 \pm 0.0005$	
O	$0.80 \pm 0.08$	$500 \pm 75$	$(1.6 \pm 0.3)\text{E}-3$	$4000 \pm 120$	$60 \pm 2$	$6.29 \pm 0.63$	$0.08 \pm 0.01$	$3.7 \pm 0.6$	$(3.3 \pm 0.8)\text{E}-4$	$0.006 \pm 0.0005$	
P	$0.70 \pm 0.07$	$500 \pm 75$	$(1.4 \pm 0.3)\text{E}-3$	$4000 \pm 120$	$60 \pm 2$	$5.88 \pm 0.59$	$0.07 \pm 0.01$	$3.3 \pm 0.6$	$(5.4 \pm 1.3)\text{E}-5$	$0.008 \pm 0.001$	
Q	–	$500 \pm 75$	–	$4000 \pm 120$	$60 \pm 2$	$4.46 \pm 0.45$	$0.06 \pm 0.01$	$1.3 \pm 0.3$	$(7.9 \pm 1.9)\text{E}-5$	$0.001 \pm 0.0001$	
R	$0.50 \pm 0.05$	$500 \pm 75$	$(1.0 \pm 0.2)\text{E}-3$	$4000 \pm 120$	$60 \pm 2$	$3.66 \pm 0.37$	$0.05 \pm 0.01$	$0.3 \pm 0.1$	$(1.4 \pm 0.4)\text{E}-5$	$0.001 \pm 0.0001$	
S	–	$500 \pm 75$	–	$4000 \pm 120$	$60 \pm 2$	$1.64 \pm 0.16$	$(2.06 \pm 0.31)\text{E}-2$	$0.12 \pm 0.02$	$(9.1 \pm 2.2)\text{E}-6$	$0.001 \pm 0.0001$	
T	$0.12 \pm 0.01$	$500 \pm 75$	$(3.0 \pm 0.5)\text{E}-4$	$4000 \pm 120$	$60 \pm 2$	$1.02 \pm 0.10$	$(1.28 \pm 0.19)\text{E}-2$	$(1.7 \pm 0.34)\text{E}-2$	$(7.1 \pm 1.7)\text{E}-7$	$0.001 \pm 0.0001$	

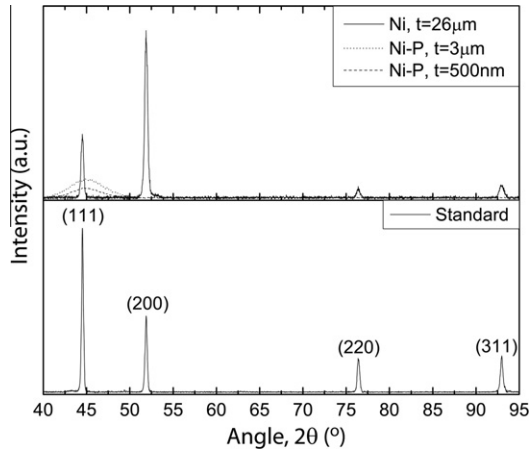


Fig. 3. XRD spectra of electroless (EN) Ni lattices with wall thickness,  $t = 500$  nm ( $\bar{\rho} = 0.19\%$ ) and  $t = 3$   $\mu\text{m}$  ( $\bar{\rho} = 0.54\%$ ), and ED Ni lattice with wall thickness,  $t = 26$   $\mu\text{m}$  ( $\bar{\rho} = 8.4\%$ ). A representative spectrum for randomly oriented polycrystalline nickel is shown for comparison.

microlattices, as film texture and microlattice symmetry are convoluted. Electron back scattered diffraction (EBSD) provides an alternative approach. Orientation maps of ED Ni films deposited on microlattices were obtained using

an FEI 3-D Quanta FEG dual beam scanning electron microscope with an acceleration voltage of 20 kV, interfaced with Oxford Instruments HKL fast acquisition software and hardware. Measurements of orientation maps were performed with a step size of 20 nm. Microlattice samples were mounted in cold mounts using Buehler EPO-THIN low-viscosity resin and its hardener (5:1.79). Mounts were polished using South Bay Technology SiC papers of 800 and 1200 grits sizes, followed by diamond suspension of 3, 1, and 0.5  $\mu\text{m}$  on velvet cloth, and colloidal silica on MultiTex cloth. Once polished, the sample was coated with a 1 nm thin layer of iridium to avoid charging and drifting interferences.

Given the difficulty in imaging the microlattice sample on a plane perpendicular to the film deposition direction, a sample with a truss angle,  $\theta = 60^\circ$ , was embedded in resin and polished on a plane oriented at  $15^\circ$  from the basal plane of the lattice ( $(x, y)$  plane in Fig. 2). This plane, oriented at  $45^\circ$  relative to the deposition direction (Fig. 5a), showed a strong (110) texture (Fig. 5b). This finding is consistent with a strong (100) texture on the deposition direction, which has been routinely observed in ED Ni films [24,28,29].

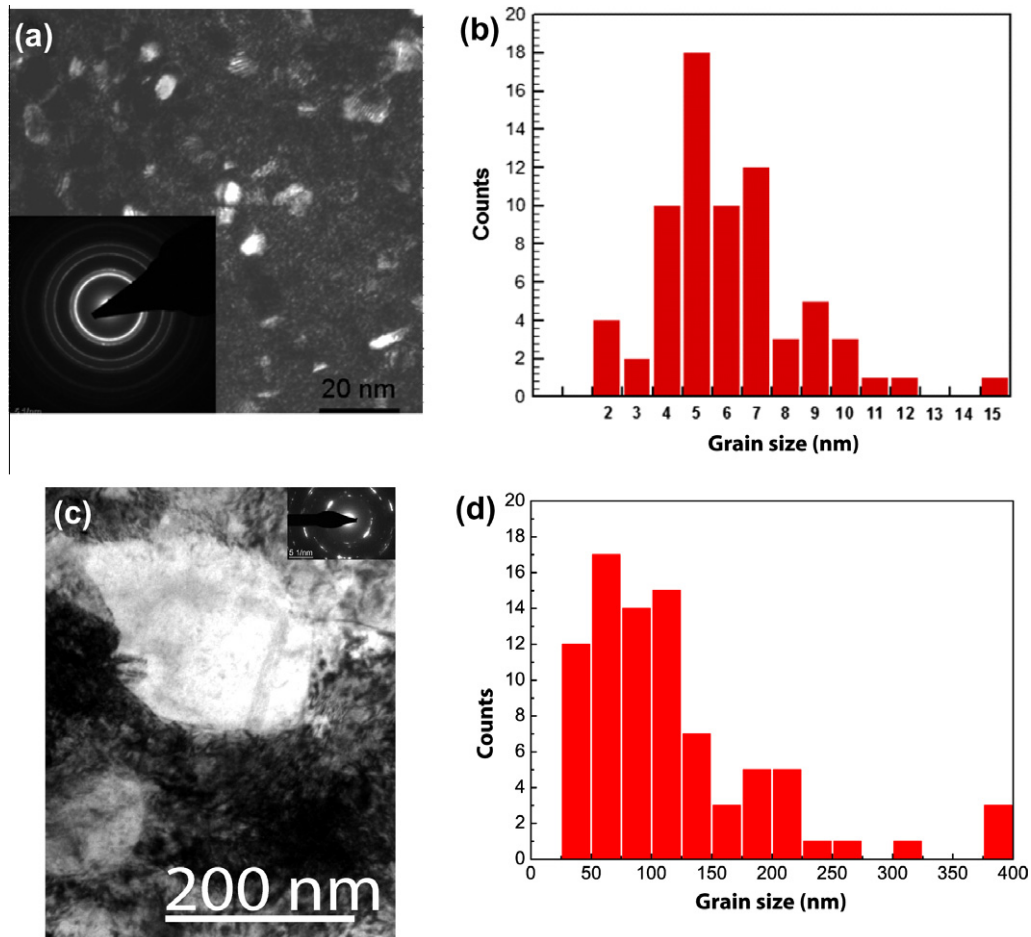


Fig. 4. Representative TEM images of electroless (EN) and electrodeposited (ED) Ni films (extracted from the lattice) with corresponding grain size distribution. (a and b) Electroless films, reprinted from Ref. [17] with permission. (c and d) Electrodeposited films.

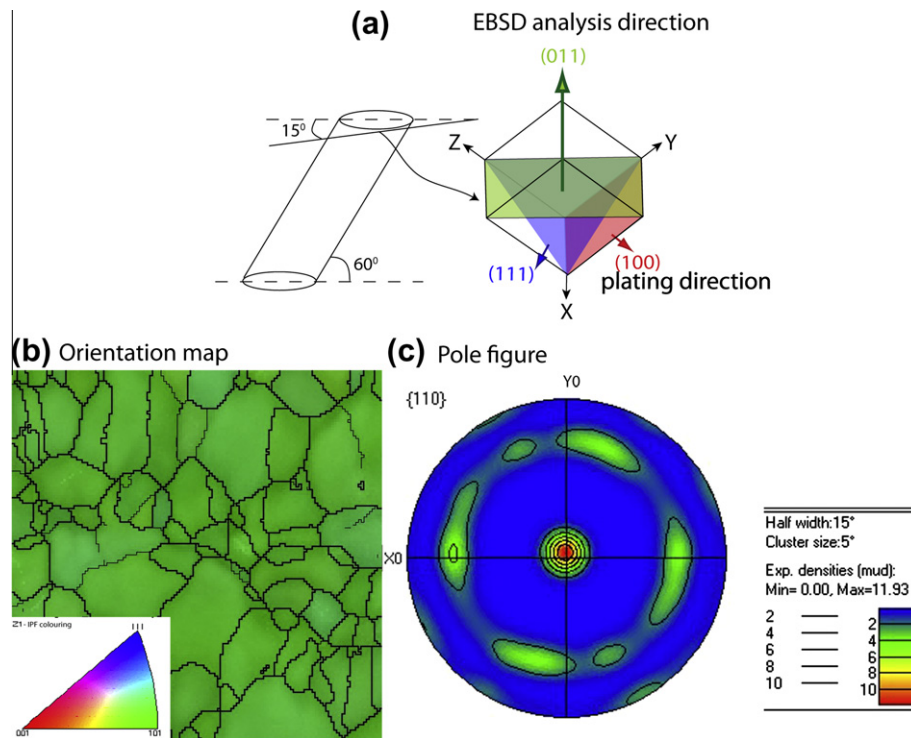


Fig. 5. (a) Schematic of a truss member of a microlattice showing that a cross-section cut at  $15^\circ$  from the horizontal provides a  $(110)$  preferential texture if the texture on a section perpendicular to the deposition direction is preferential along  $(100)$ . (b) Orientation map of the  $15^\circ$  cross-section showing that all the crystals are oriented along the  $(110)$  direction; and (c) associated pole figure showing clear texture along the  $\{110\}$  family of planes.

## 4. Mechanical characterization

### 4.1. Measurement of base materials properties

The nanoscale mechanical response of EN Ni films identical in composition to those described in this work, both deposited on flat substrates and in the form of hollow cylinders, has been recently published [17]. A hardness  $H$  of  $\sim 6.3$  GPa was measured by nanoindentation on flat films. Indentation of EN Ni solid nanopillars with diameters ranging from 500 nm to 1500 nm yielded  $H = 7.8$ – $8.1$  GPa, showing minimal film thickness dependence. These results combined indicate an average yield strength,  $\sigma_Y^{EN} \sim H/3 = 2.5$  GPa, roughly independent on the wall thickness. Nanoindentation on ED Ni films (thickness between 5 and 15  $\mu\text{m}$ ) deposited on flat substrates provide a hardness of 2.9 GPa [30]. The well-known correlation  $\sigma_Y = H/3$  has been shown to generally overpredict the yield strength in electrodeposited nanocrystalline nickel, with most experimental results in the range  $\sigma_Y = H/4$ – $H/3$ , from which we extract a yield strength,  $\sigma_Y^{EN} = 0.75$ – $0.9$  GPa. Nanoindentation is not the ideal technique for the extraction of the Young's modulus of sub-micron-thick films, due to a very non-uniform stress field and the presence of a strong substrate effect [31]. Uniaxial compression of hollow EN Ni cylinders of similar diameters as the truss members considered in this work and thicknesses of 150 and 500 nm provided a more accurate measurement of  $E^{EN} = 210$  GPa [17]. The same value is assumed to be a

good estimate for electrodeposited films as well, in good agreement with literature data. Hence in the following analysis we will use  $E^{ED} = 210$  GPa.

### 4.2. Macroscale mechanical response

#### 4.2.1. Methods

The macroscopic mechanical behavior of nickel microlattices of different wall thickness and unit cell sizes was investigated by quasi-static axial compression experiments. All tests were performed with a servo-electric INSTRON 8862 frame, equipped with a FastTrack 8800 controller and a National Instrument SCXI Data Acquisition system. The displacement rate was accurately controlled at  $10 \mu\text{m s}^{-1}$  for all tests. The load,  $P$ , was measured using SENSOTEC load cells, with ranges of 250 N and 250 lb, depending on the sample tested; the displacement,  $\delta$ , was measured by the internal LVDT embedded in the frame actuator. As the accuracy of the internal LVDT in providing sample strain depends on the magnitude of the applied load, an external LVDT was used for modulus extraction. Engineering stress and strain were used throughout, defined as  $\sigma = P/A_0$  and  $\varepsilon = \delta/L_0$ , with  $A_0$  and  $L_0$  the initial cross-sectional area and length of the sample, respectively. The samples were not attached to face sheets or compression platens on either the top or the bottom. Strain–stress curves were analyzed to extract the modulus of elasticity,  $E$ , the yield stress,  $\sigma_Y$ , the maximum stress,  $\sigma_{max}$ , and the energy loss coefficient,  $\Delta U/U$ , calculated by dividing the

absorbed energy by the total energy required for compression. For all measured quantities, the scatter among nominally identical samples is much larger than the instrumentation error, and is reported in Table 1; where no repeated tests are available, the error is assumed equal to that of the sample of closest density. The energy loss coefficient has error comparable to that of the strength,  $\sim\pm 10\%$ . A similar error is conservatively assumed for the residual strain.

#### 4.2.2. Deformation mechanisms

The macroscale compressive response of microlattices with different geometric parameters and densities (Samples T, J, C, and A in Table 1) is depicted in Fig. 6. For all densities, the loading response consists of an elastic portion followed by a fairly constant plateau. Conversely, the unloading behavior is a dramatic function of the relative density. In the ultra-light regime (EN Ni,  $\bar{\rho} = 0.01\%$ , Fig. 6a), nearly complete recovery is obtained after a compressive strain of 25%. A subsequent cycle will show a decrease in the elastic modulus and the plateau stress (evidence of damage occurred during the first cycle), but a nearly identical unloading path. For EN Ni samples at a relative density,  $\bar{\rho} = 0.19\%$  (Fig. 6b), the first loading/unloading cycle is similar to that of ultra-light lattices (Fig. 6a), and nearly total recovery is obtained after 50% compressive strain. The second loading/unloading cycle is very different from the first one, though, an obvious indication of substantial damage suffered during the first cycle. Nonetheless, the peak stress at 50% strain is only 10%

lower than for the first cycle. Loading/unloading cycles following the second one are nearly self-similar, showing evidence of little subsequent damage. The behavior after the second cycle qualitatively resembles that of non-linear visco-elastic materials [32] including forests of carbon nanotubes [33], although the deformation mechanisms (elaborated below) are obviously different. If the relative density is further increased (EN Ni,  $\bar{\rho} = 0.54\%$ , Fig. 6c and ED Ni,  $\bar{\rho} = 8.4\%$ , Fig. 6d), the behavior becomes similar to that of conventional metallic cellular materials, with an elastic phase, a plateau phase and nearly no elastic recovery upon unloading.

To uncover the effect of the maximum compressive strain on the response to cyclic loads, three pristine nominally identical samples (Samples M, L and J in Table 1, with the same geometry as for Fig. 6b) were subjected to five loading/unloading cycles, with maximum strains of 4%, 10% and 50%, respectively. The results are depicted in Fig. 7. At 4% strain (Fig. 7a), the load is removed right before the occurrence of a peak, and all the five cycles are self-similar (albeit with some evidence of minor damage after the first cycle). If the sample is strained to 10% (Fig. 7b), a shallow load drop is observed after the peak, and the unloading response is almost bi-linear (a shallow load drop followed by a sharper one, with a transition at  $\sim 2\%$  strain). Cycles after the second one are self-similar, with some evidence of damage accumulation. For extremely large maximum strain (50%, Fig. 7c), in the first loading cycle the peak stress and the subsequent drop are followed by a nearly constant plateau. The unloading

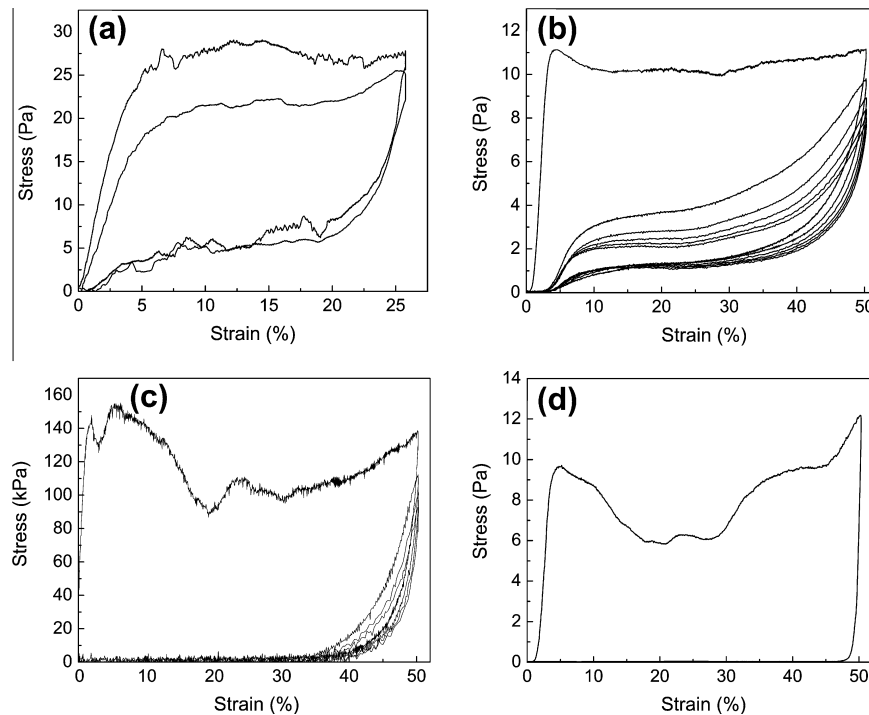


Fig. 6. Compressive response of microlattices (Samples T, J, C and A from Table 1, respectively) at progressively increasing wall thickness: (a)  $t = 150$  nm (EN Ni), (b)  $t = 500$  nm (EN Ni), (c)  $t = 3$   $\mu\text{m}$  (EN Ni), and (d)  $t = 26$   $\mu\text{m}$  (ED Ni). In (a–c), unload–reload cycles are shown. Modified from Ref. [14].

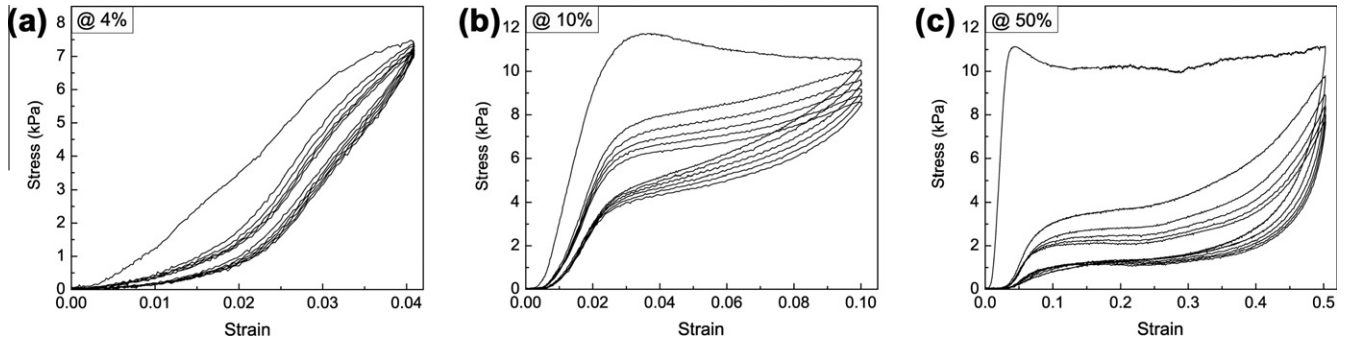


Fig. 7. Response of an EN Ni lattice (Samples M, L, and J in Table 1) to cyclic compressive loads, for different values of the maximum applied strain: (a) 4%, (b) 10%, (c) 50%.

response now shows a tri-linear behavior: a very sharp stress drop, followed by a long, almost constant plateau, and a final drop near the origin.

The evolution of elastic modulus, yield strength, plateau stress and loss coefficient upon mechanical cycling for the three load cases depicted in Fig. 7 is plotted in Fig. 8. Notice that in all cases, all properties drop significantly after the first cycle, but substantially stabilize after the second cycle. Not surprisingly, the magnitude of the drop after the first cycle (indicative of the amount of damage suffered by the material) strongly increases with increased maximum compressive strain. The erratic behavior displayed by the elastic modulus at 4% strain (Fig. 8a) is most likely due to the difficulty in extracting representative moduli at low strain in ultra-light cellular materials, where edge effects (e.g., deformation of the truss elements at the boundary) are significant. To minimize these effects, for all load cycles, the elastic modulus has been extracted after the slope has stabilized, rather than at the origin.

The energy loss coefficients plotted in Fig. 8 are particularly remarkable, as they stabilize to  $\sim 0.2$  for all maximum strains under investigation. For comparison, pure nickel ( $>99\%Ni$ ) has a maximum loss coefficient of 0.0032 [34], whereas the lossiest nickel foams (INCO TYPE) top at  $\sim 0.02$  [1]. Hence the unique ultra-light architecture imparts exceptional damping performance to these materials, unprecedented for any metallic system.

Collectively, all the data presented above strongly suggest that irreversible deformation mechanisms only occur upon first loading, with subsequent cycles exhibiting nearly elastic, recoverable behavior. This is consistent with nodal fracture events occurring sequentially, and exclusively during the plateau phase of the loading cycle. A direct confirmation of this hypothesis is presented in Fig. 9. In Fig. 9a, a pristine sample (Sample K in Table 1, ED Ni,  $\bar{\rho} = 0.09\%$ ) was subjected to five compressive cycles, at progressively increasing maximum strain. Each new cycle shows evidence of damage from the previous cycle and introduces additional damage in the plateau phase. Subsequently, the same sample is subjected to another series of five compressive cycles, with exactly the same progression of maximum strain as in Fig. 9a. The results (Fig. 9b) clearly show no additional damage.

Scanning electron microscopy (SEM) images of post-mortem samples (Fig. 10) help gain further insight on the deformation mechanism. For ultra-light samples (Sample J, EN Ni,  $\bar{\rho} = 0.19\%$ ), cracks at nodes are clearly visible (Fig. 10a). Notice that these cracks do not extend entirely through the node, and intact ligaments remain. We surmise that by virtue of their thickness, the intact ligaments allow extensive rotation of the members without the introduction of plastic strain, thereby allowing reversible behavior at enormous macroscale compressive strains after cracking. Although nodal cracks remain evident in thicker samples,

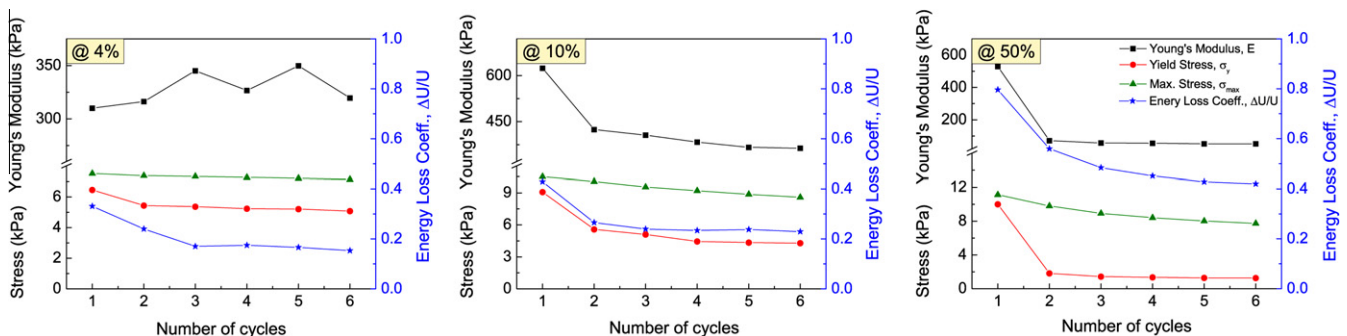


Fig. 8. Evolution of the mechanical properties for the cyclic compression tests illustrated in Fig. 7. Notice that the first cycle induces damage in the material (as indicated by a drop in all properties), which is more substantial at larger maximum strains, but the behavior generally stabilizes after the second cycle.

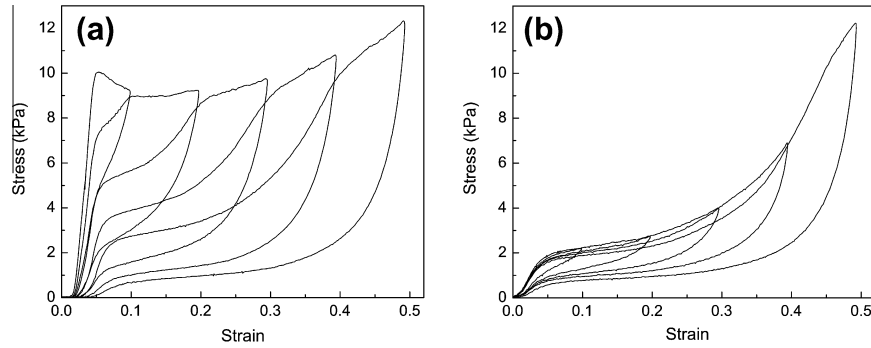


Fig. 9. (a) Compressive response of a pristine EN Ni microlattice (Sample K in Table 1) under cyclic loads of progressively larger strain amplitude. (b) Compressive response of the same material, re-loaded through the same sequence of cycles after the last cycle in (a). Notice that subsequent cycles at strain lower than the maximum strain ever applied on the material induce minimal damage on the material.

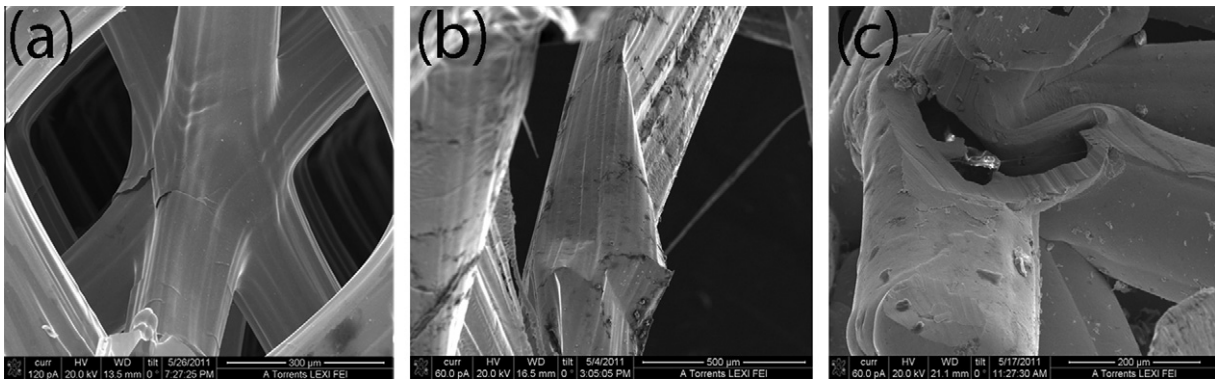


Fig. 10. SEM images of microlattices (Samples J, E and A in Table 1) of different wall thickness after testing at 50% strain. From left to right:  $t = 500$  nm (EN Ni,  $\bar{\rho} = 0.19\%$ ),  $t = 1.3$   $\mu\text{m}$  (EN Ni,  $\bar{\rho} = 0.28\%$ ), and  $t = 26$   $\mu\text{m}$  (ED Ni,  $\bar{\rho} = 8.4\%$ ). Notice partial fracture at a node (a), localized (Brazier) buckling (b), and plastic hinging at a node (c).

other mechanisms appear. For slightly thicker samples (Sample E, EN Ni,  $\bar{\rho} = 0.28\%$ ), local plastic buckling (in the form of kinking, induced by Brazier buckling [35]) is evident (Fig. 10b). Finally, much thicker samples (Sample A, ED Ni,  $\bar{\rho} = 8.4\%$ ) show the typical extensive plastic deformation at nodes that is expected in conventional foams and lattice materials (Fig. 10c). Post-mortem images of samples that have not undergone plastic deformation cannot provide evidence of elastic buckling. To ascertain the presence of this deformation mode, an ultra-light sample (Sample G, EN Ni,  $\bar{\rho} = 0.21\%$ ) was compressed to 50% strain and embedded in epoxy resin in situ, thus “freezing” the deformed shape. Given the low shrinkage of the resin upon curing (Buehler Epothin low viscosity resin with a reported linear shrinkage,  $\Delta L/L = 10^{-4}$ ), and the extremely low strain energy in the sample, the “frozen shape” upon removal from the test frame is essentially identical to that before embedding. Optical images (Fig. 11) reveal the presence of kinking at the nodes, similar in shape to the plastic kinking observed in Fig. 10b for thicker samples. Also evident from Fig. 11 is the extensive rotation that truss members undergo, with minimal bending. As mentioned above, this is enabled by partial cracking at nodes (Fig. 10a) and kinking induced by Brazier elastic buckling, either at nodes or by the center of the members (Figs. 10b and 11). Based

on these two mechanisms, a simple mechanical analysis (Appendix) predicts a transition from the elastic recovery regime to the plastic regime at a critical wall-thickness-to-diameter ratio given by:

$$\left(\frac{t}{D}\right)_{cr} \sim \frac{\sigma_{Y,s}}{E_s} \frac{0.25}{\theta - \sin^{-1}[(1 - \varepsilon_{max}) \sin \theta]} \quad (1)$$

with  $\sigma_{Y,s}$  and  $E_s$  the base material yield strength and elastic modulus, respectively;  $\theta$  the truss angle (Fig. 2); and  $\varepsilon_{max}$  the maximum compressive strain. For EN Ni lattices (properties in Section 3.1) with  $\theta = 60^\circ$  and  $\varepsilon_{max} = 50\%$ , we predict  $(t/D)_{cr} = 0.005$ . Fig. 12 depicts the residual strain after 50% compression (first cycle) for a number of samples. A transition from a fully recoverable deformation mode to a plasticity-governed regime is evident. The factor five discrepancy between the model and the experimental data is attributed to strain localization, which is ignored in the model. Fig. 11 clearly reveals that the deformation of the microlattice is not uniform across the thickness: one side (in this case the upper side) fails first (possibly due to slight tapers in the member thickness or diameter), and the deformation progresses sequentially in a layer-by-layer mode. In spite of this discrepancy, Eq. (1) clearly captures the order of magnitude of the transition and can be used as a simple tool for the design of microlattices with

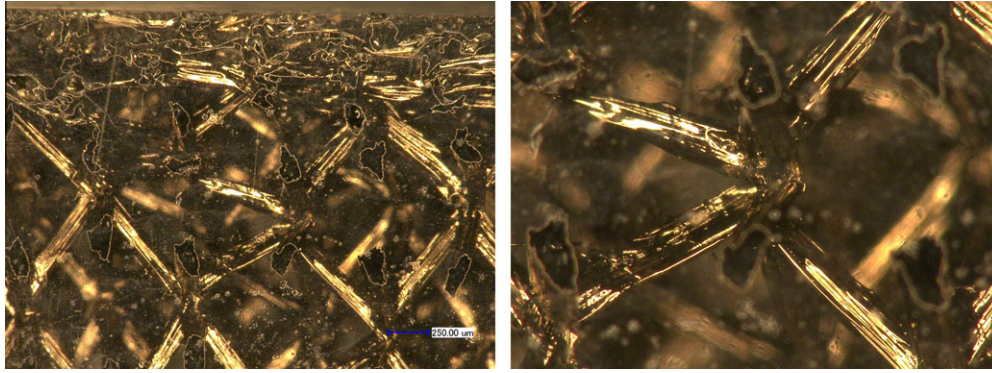


Fig. 11. Optical images of a polished cross-section of a microlattice (Sample G in Table 1) of wall thickness,  $t = 550$  nm, which was previously embedded in epoxy in situ at a 50% compressive strain (effectively “freezing” the deformed shape). The right image is a close-up around a node. Notice that the truss members undergo large rotation at the nodes (facilitated by partial nodal fracture and/or Brazier buckling) while remaining virtually straight (and hence largely unloaded) through most of their length. Also notice that the deformation is not uniformly distributed across the sample thickness, with the layers on top almost fully densified and those at the bottom almost unstrained.

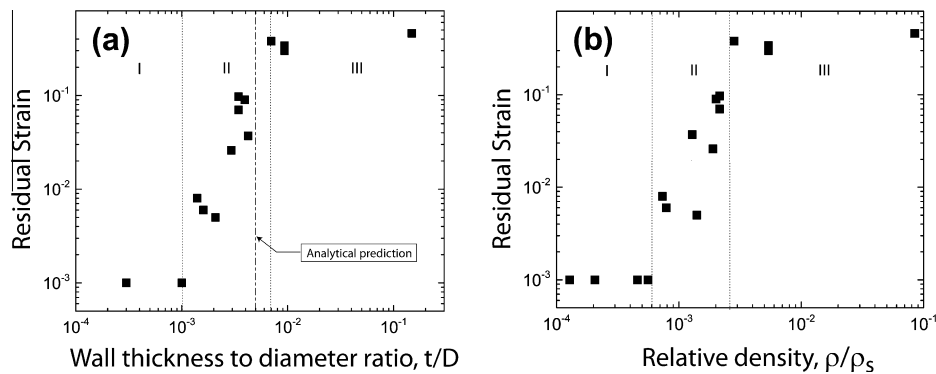


Fig. 12. Residual strain vs. wall thickness to diameter ratio (a) and relative density (b) after the first compression cycle at 50% strain amplitude for a number of microlattices spanning three decades in relative densities. A clear transition from a fully recoverable deformation mode (regime I) to a plasticity governed behavior (regime III) occurs at  $t/D = 0.001$ – $0.008$ , corresponding to densities of  $\sim 0.06$ – $0.3$ . A simple analytical model (Eq. (1)) captures the order of magnitude of the critical  $t/D$ .

desired amounts of strain recovery (and associated damping characteristics).

## 5. Mechanical efficiency

The mechanical efficiencies of nickel microlattices can be illustrated by cross-plotting compressive modulus and strength (normalized with the properties of the base metal – see Section 3.1) as a function of the relative density.

The experimental data for the Young’s modulus (Fig. 13a) show a  $\bar{\rho}^2$  scaling, in perfect agreement with a metal foam model [2], through the entire range of relative densities. Moduli extracted from the loading and unloading segments of the stress–strain curve are extremely similar. A foam-like scaling for the modulus of topologically ordered lattice materials is at first surprising, as the design of stretching-dominated lattices generally results in a linear scaling (and hence much superior performance) [7,8]. The reason for the observed behavior is twofold: (i) the lattice under consideration is not stretch-dominated, due to the lack of truss members in the horizontal plane (the  $(x, y)$  plane in Fig. 2); (ii) most of the deformation is concentrated at the

nodes, as opposed to being distributed along the truss members. The two phenomena combined are consistent with the observed scaling. A subsequent study will address the quantitative details. In spite of the different scaling behavior of hollow microlattices as compared to stretch-dominated macroscale lattices, a remarkable feature emerges: the scaling of the modulus with relative density does not change in the ultra-light regime (density  $< 0.1\%$ ). Two characteristic materials that exist at relative densities below 1% (carbon nanotube foams and aerogels) exhibit scalings  $\sim \bar{\rho}^3$  [36,37]. Furthermore, no cellular materials besides silica aerogels have been reported at relative densities below 0.1%. The implication is that the EN Ni microlattices described in this work are the stiffest materials with densities below  $10 \text{ mg cm}^{-3}$  [14].

The trend exhibited by the compressive strength is more complex (Fig. 13b). Denser, ED microlattices ( $\bar{\rho} = 10\%$ ) agree very well with metal foam models [2]. (If the lower bound for the base material strength is used (Section 3.1), the behavior of the microlattices is slightly superior.) Once again, this is consistent with a plasticity-dominated behavior initiated by bending at the nodes. EN Ni microlattices

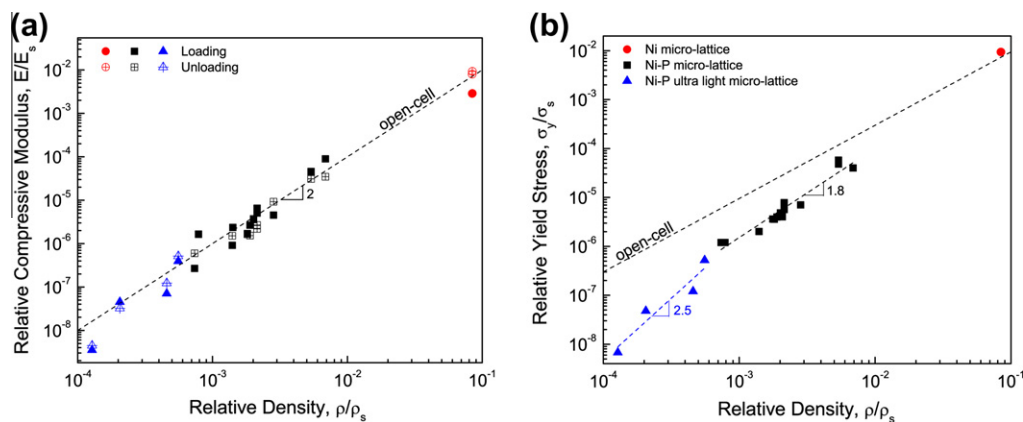


Fig. 13. Relative compressive modulus (a) and yield strength (b) as functions of the relative density for a number of microlattices spanning three orders of magnitude in density (see Table 1 for sample dimensions). The red dot at  $\sim 10\%$  density represents an ED Ni lattice, whereas the rest of the data points are for EN Ni samples. The blue triangles represent ultra-light lattices (density  $< 0.1\%$ ). Remarkably, for all lattices the relative modulus scales quadratically with the relative density, as for stochastic foams. In strength, the ED sample agrees well with a foam model, whereas EN lattices in the density range 0.1–1% show nearly the same scaling, but exhibit a knock-down factor of  $\sim 2$ –5. In the sub-0.1% range, the scaling changes to a much steeper exponent, indicative of a switch in the deformation mode. This switch is consistent with the elastic-to-plastic transition depicted in Fig. 12b. (For interpretation of the references to color in this figure legend, the reader is referred to the web version of this article.)

at densities  $\sim 0.1$ –1% exhibit strength that scales as  $\bar{\rho}^{1.8}$ , still in acceptable agreement with open-cell stochastic foams (albeit with a knock-down factor, tentatively attributed to node fracturing and deformations concentrated around the nodes). For densities lower than 1%, though, the strength scaling for EN Ni microlattices sharply changes to  $\bar{\rho}^{2.5}$ . The transition is perfectly consistent with the sharp change in deformation mode depicted in Fig. 12b, clearly revealing that this change in scaling marks a shift from a plasticity-dominated deformation mode ( $\bar{\rho} > 0.1\%$ ) to a regime characterized by local elastic buckling and brittle fracture at the nodes ( $\bar{\rho} < 0.1\%$ ). Future assessments will provide mechanistic models for these deformation modes.

In spite of the knock-down factors introduced by topological effects (the bending-dominated nature of the lattice and the localization of the deformation at the nodes), microlattices are superior to commercially available Ni foams of comparable densities, by virtue of the superior base material strength imparted by the nano-crystalline microstructure of the film: as a result, a 8.4% dense ED Ni microlattice has a compressive yield strength of 8.51 MPa, whereas an INCO nickel foam of the same density has a strength of 2.57 MPa [38]. Modifications in lattice topology and careful node design, informed by optimization studies, could further improve the benefit: such studies are currently being conducted.

## 6. Conclusions

Novel nickel-based microlattice materials with structural hierarchy spanning three different length scales (nm,  $\mu\text{m}$ , mm) were manufactured, and characterized microstructurally and mechanically. These materials are produced by plating a sacrificial template obtained by self-propagating photopolymer waveguide prototyping. Ni–P films with a thickness of 120 nm to 3  $\mu\text{m}$  are deposited by

electroless plating, whereas thicker films (5–26  $\mu\text{m}$ ) are obtained by subsequent electroplating of a pure Ni layer. This results in samples spanning three orders of magnitude in relative density, from 0.01% to 8.4% (Table 1).

Microstructural characterization via XRD and TEM reveals that the thin EN Ni films have ultra-fine grain size (7 nm) and a yield strength of  $\sim 2.5$  GPa. Conversely, the thicker ED Ni films exhibit a much broader distribution with average grain size of 116 nm and strong (100) texture in the plating direction, resulting in a yield strength of  $\sim 1$  GPa. The elastic modulus is quite similar for both base materials ( $E \sim 210$  GPa).

Uniaxial compression experiments reveal two distinct mechanical responses. At ultra-low densities ( $< 0.1\%$ ), these lattices exhibit nearly full recovery after strains as large as 50%, and damping coefficients an order of magnitude larger than for conventional Ni foams. This behavior is unprecedented for any metallic system. At higher densities (0.1–10%), the compression behavior is fully plastic, similarly to traditional cellular metals. Optical and electron imaging of deformed lattices show that the deformation largely localizes around the nodes. The pseudo-super-elastic behavior for ultra-low-density lattices is attributed to nodal fracture events and local elastic buckling (kinking), which allow extensive rotation around thin ligaments without the introduction of plastic strain. A simple mechanical model based on this observation clearly captures the order of magnitude of the critical-thickness-to-diameter ratio for the transition, and may be used to design microlattices with desired recovery and damping characteristics. Although the deformation localization at the nodes limits the achievable stiffness and strength, it may be beneficial for energy absorption applications, where nodal deformation reduces the large difference between the peak transmitted stress and the average plateau stress [4]. In the ultra-light regime, the microlattice materials characterized in this work are

approximately one order of magnitude stiffer and stronger than any existing alternative, and even at large densities (8.4%) they are three times stronger than nickel foams of comparable weight. These substantial benefits stem from the hierarchical nature of the lattice topology, which allows capitalization of plasticity size effects in a macroscale structural material.

### Acknowledgements

This material was supported by the Defense Advanced Research Projects Agency (DARPA) under the Materials with Controlled Microstructural Architecture program managed by Dr. Judah Goldwasser (contract no. W91 CRB-10-0305). We are indebted to J. Lian and J.R. Greer for performing nanoindentation measurements and providing constructive criticism on the manuscript. We would also like to thank J. W. Hutchinson for thoughtful discussions, and acknowledge the LEXI laboratories facilities located in the Calit2 building at University of California, Irvine.

Thanks are extended to Anh Duong and Shehreen Dheda for their technical assistance with FIB and TEM.

### Appendix A. A simple model for elastic recovery

In situ and post-mortem images of ultra-low-density microlattices (Figs. 10 and 11) clearly show that extremely large strains (50%) are accommodated by extensive rotation at the nodes, with the truss members only exhibiting minimal deformation. Consistent with observations, two mechanisms are surmised: (i) partial fracture of a node with subsequent rotation about a remnant ligament; (ii) elastic kinking at the node (induced by Brazier buckling) and subsequent rotation about the kink. In both cases, the rotation occurs by bending a thin film of thickness  $\sim t-2t$  (with  $t$  the wall thickness of the truss member) and length of the order of the truss member radius,  $D/2$  (Fig. A1a). Assuming a uniform deformation through the sample, the rotation  $\alpha$  required to accommodate a global strain  $\epsilon_{max}$  can be expressed geometrically as:

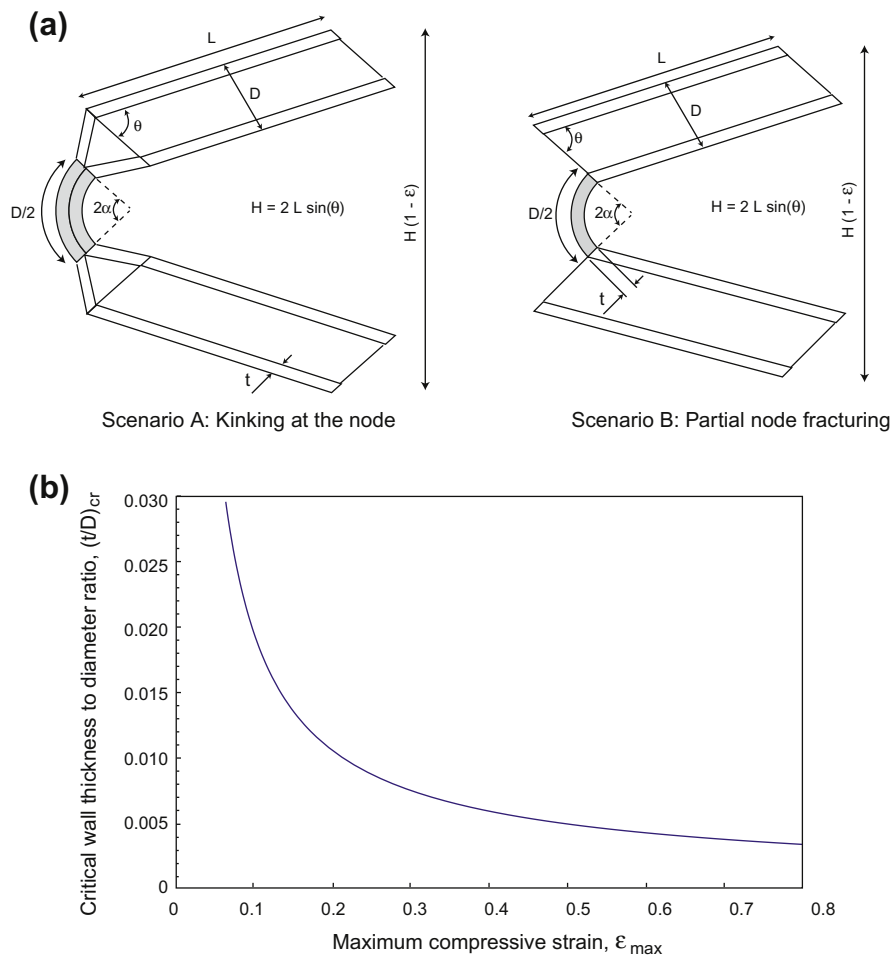


Fig. A1. (a) Schematic of two nodal deformation modes that would result in large global strain without introducing plastic strain. (b) Maximum wall thickness to diameter ratio to enable full recovery from a given global compressive strain, according to a simple theory based on the mechanisms depicted in (a).

$$\alpha = \theta - \sin^{-1}[(1 - \varepsilon_{max}) \sin \theta] \quad (\text{A1})$$

where  $\theta$  is the truss angle.

This rotation induces a curvature in the film,  $\kappa = 4\alpha/D$ . The critical condition for elastic recovery is obtained by imposing that the film be at the verge of yielding, i.e.:

$$k_{cr} = \frac{M_y}{E_s I} = \frac{\sigma_{Y,s}}{E_s t} \quad (\text{A2})$$

This condition can be expressed in terms of a critical-wall-thickness-to-diameter ratio,  $(t/D)_{cr}$ , as:

$$\left(\frac{t}{D}\right)_{cr} \sim \frac{\sigma_{Y,s}}{E_s} \frac{0.25}{\theta - \sin^{-1}[(1 - \varepsilon_{max}) \sin \theta]} \quad (\text{A3})$$

with  $\sigma_{Y,s}$  and  $E_s$  the compressive yield strength and Young's modulus of the base material, respectively. This critical ratio is plotted in Fig. A1b.

## References

- [1] Ashby MF, Evans AG, Fleck NA, Gibson LJ, Hutchinson JW, Wadley HNG. Metal foams: a design guide. Oxford: Butterworth-Heinemann; 2000.
- [2] Gibson LJ, Ashby MF. Cellular solids: structure and properties. Cambridge: Cambridge University Press; 1999.
- [3] Wadley HNG. Adv Eng Mater 2002;4:726.
- [4] Evans AG, He MY, Deshpande VS, Hutchinson JW, Jacobsen AJ, Carter WB. Int J Imp Eng 2010;37:947.
- [5] Lu TJ, Valdevit L, Evans AG. Prog Mater Sci 2005;50:789.
- [6] Valdevit L, Jacobsen AJ, Greer JR, Carter WB. J Am Ceram Soc Bull 2011;94:S15.
- [7] Deshpande VS, Fleck NA, Ashby MF. J Mech Phys Solids 2001;49:1747.
- [8] Evans AG, Hutchinson JW, Fleck NA, Ashby MF, Wadley HNG. Prog Mater Sci 2001;46:309.
- [9] Wadley HNG. Philos Trans Royal Soc A 2006;364:31.
- [10] Greer JR, De Hosson JTM. Prog Mater Sci 2011;56:654.
- [11] Koch CC. Structural nanocrystalline materials: fundamentals and applications. Cambridge: Cambridge University Press; 2007.
- [12] Gordon LM, Bouwhuis BA, Surlavo M, McCrea JL, Palumbo G, Hibbard GD. Acta Mater 2009;57:932.
- [13] Jacobsen AJ, Barvosa-Carter W, Nutt S. Adv Mater 2007;19.
- [14] Schaedler TA, Jacobsen AJ, Torrents A, Sorensen AE, Lian J, Greer JR, et al. Science 2011;334(6058):962.
- [15] Jacobsen AJ, Barvosa-Carter W, Nutt S. Acta Mater 2007;55:6724.
- [16] Jacobsen AJ, Barvosa-Carter W, Nutt S. Acta Mater 2008;56:2540.
- [17] Lian J, Jang D, Valdevit L, Schaedler TA, Jacobsen AJB, Carter W, et al. Nano Lett 2011;11:4118.
- [18] Kulg KP, Alexander LE. X-ray diffraction procedures. New York: John Wiley & Sons; 1974.
- [19] Djokic SS, Djokić SS, Cavallotti PL. Electrodeposition. Electroless deposition: theory and applications, vol. 48. New York: Springer; 2010. p. 251.
- [20] Kumar PS, Nair PK. J Mater Process Technol 1996;56:511.
- [21] Chauhan M, Mohamed FA. J Mater Sci 2007;42:1606.
- [22] Godon A, Creus J, Feugas X, Conforto E, Pichon L, Armand C, et al. J Mater Charact 2011;62:164.
- [23] He J, Ye J, Lavernia EJ, Matejczyk D, Bampton C, Schoenung JM. J Mater Sci 2004;39:6957.
- [24] Torrents A, Yang H, Mohamed FA. J Metall Mater Trans A 2010;41A:621.
- [25] Dalla Torre F, Van Swygenhoven H, Schaublin R, Spatig P, Victoria M. Scripta Mater 2005;53:23.
- [26] El-Sherik AM, Erb U. Page J Surf Coat Technol 1996;88:70.
- [27] Rashidi AM, Amadeh A. J Surf Coat Technol 2008;202:3772.
- [28] Rashidi AM, Amadeh A. J Mater Sci Technol Ser 2010;26:82.
- [29] Dini JW. Electrodeposition – the materials science of coatings and substrates. Park Ridge, NJ: Noyes Publications; 1993.
- [30] Lian J, Greer JR. Unpublished results.
- [31] Fischer-Cripps AC. Nanoindentation. New York: Springer; 2010.
- [32] Lakes RS. Viscoelastic materials. Cambridge: Cambridge University Press; 2009.
- [33] Cao AY, Dickrell PL, Sawyer WG, Ghasemi-Nejhad MN, Ajayan PM. Science 2005;310:1307.
- [34] IMMA handbook of engineering materials. Parkville (Victoria): Institute of Metals and Materials Australasia; 1997.
- [35] Calladine CR. Theory of shell structures. Cambridge: Cambridge University Press; 1983.
- [36] Ma H, Prevost J, Jullien R, Scherer G. J Non-Cryst Solids 2001;285:216.
- [37] Worsley MA, Kucheyev SO, Satcher JH, Hamza AV, Baumann TF. Appl Phys Lett 2009;94:073115.
- [38] Queheillalt DT, Katsumura Y, Wadley HNG. Scripta Mater 2004;50:313.